Selective stacking in the reflection-angle and azimuth domain

Yaxun Tang

ABSTRACT

I analytically demonstrate the existence of artifacts in angle-domain common-image gathers (ADCIGs) caused by sparsely sampled wavefields from the perspective of shot-profile migration. The subsurface-offset domain common-image gather (SODCIG) is linearly related to the ADCIG in locally constant-velocity media when the wavefields are sufficiently well sampled, but not when the wavefields are poorly sampled. Hence, linear slant-stack or radial-trace transform in SODCIGs will produce ADCIGs with artifacts, which might hinder further interpretation or analysis and reduce the quality of the final stacking image. Instead of simply stacking along reflection angle and azimuth axes, I present a method to compute the stacking weights as functions of angle and azimuth and make the stacking process selective. My method is tested on the synthetic wide-azimuth version of the SEG/EAGE salt data set, where a cleaner image with higher signal-to-noise ratio is obtained.

INTRODUCTION

Seismic image quality is highly dependent on the acquisition geometry, or more specifically, on the illumination of the subsurface. Ideally, the best image is obtained when each subsurface image point is illuminated equally, which potentially requires a recording geometry both finely sampled and infinite in length. In the real world, however, we always have a limited recording geometry. For example, in the standard marine-streamer acquisition system, only narrow-azimuth data with limited offsets are acquired. Recent developments in multi-azimuth or wide-azimuth acquistion techniques (Michell et al., 2006; Keggin et al., 2006; Howard and Moldoveanu, 2006) provide a richer coverage in azimuth, and the subsurface can be better illuminated, especially in subsalt areas. Much better images are obtained because of improved subsurface illumination. Nevertheless, the reality can never meet the requirement for infinite recording geometry and infinitly dense sampling for shots and receivers. Illumination holes and aliasing may still happen in complex geologies. Poor illumination results in poor images, and related artifacts destort the migrated image, making it difficult to interpret. This effect is readily visible in the reflection-angle and azimuth domain, where illumination holes and related artifacts can be identified. They are by no means random or weak, and thus simple stacking can not attenuate them effectively.

In this paper, I briefly review methods for extracting subsurface-offset-domain common-image gathers (SODCIGs) and angle-domain common-image gathers (ADCIGs). I demon-

strate the effects of sparsely sampled wavefields on both SODCIGs and ADCIGs. I also demonstrate that the final image formed by simply stacking over the reflection-angle and azimuth axes without any weighting function suffers from artifacts caused by the poor illumination and has a low signal-to-noise ratio. Instead, I describe a simple but effective way to make the stacking process selective: we stack only those reflection angles and azimuths with good illumination. This method is tested on the wide-azimuth version of the SEG/EAGE salt data set, and a better image with higher signal-to-noise ratio is obtained.

EXTRACTING ANGLE-DOMAIN COMMON-IMAGE GATHERS

ADCIGs can be extracted either before applying an imaging condition (Prucha and Symes, 1999; Mosher and Foster, 2000; Xie and Wu, 2002; Soubaras, 2003) or afterward (Sava and Fomel, 2003; Biondi and Symes, 2004). The advantage of extracting the angle gathers after the imaging step is that it is a model-space processing, which offers more versatility and generally more efficiency. The same transformation can be used for images produced by source-receiver migration (Sava and Fomel, 2003), shot-profile migration (Rickett and Sava, 2002) and reverse time migration (Biondi and Shan, 2002).

There are basically two steps to extract the angle gathers after imaging: First, compute the SODCIGs. Second, transform the SODCIGs into ADCIGs. For source-receiver migration, the SODCIGs are immediately available after downward continuation of the wavefields; for shot-profile migration, a multi-offset imaging condition should be applied to get the SODCIGs (Rickett and Sava, 2002):

$$I(x,y,h_x,h_y) = \sum_{\omega} D^*(x-h_x,y-h_y,\omega)U(x+h_x,y+h_y,\omega), \tag{1}$$

where I is the image in the subsurface-offset domain, D is the source wavefield, * means the complex conjugate, U is the receiver wavefield, x, y are the components of midpoint, h_x, h_y are the components of subsurface half offset, and ω is frequency. Sava and Fomel (2003) derived the following radial-trace transformation in the Fourier domain to transform the SODCIGs into ADCIGs in 2-D:

$$\tan\gamma = -\frac{k_{h_x}}{k_z} = -\frac{\partial z}{\partial h_x}, \tag{2}$$

where γ is the reflection angle, k_{h_x} is the offset wavenumber, and k_z is the depth wavenumber. The transformation is independent of geological dip in 2-D, but the 3-D formulation must be corrected for a crossline dip component. Tisserant and Biondi (2003) show that we can make this 3-D correction by re-writing the angle-gather transformation as

$$\tan\gamma = -\frac{|\mathbf{k_h}|}{k_z}\frac{1}{\sqrt{1+\left(\frac{k_{m_x}}{k_z}\sin\beta + \frac{k_{m_y}}{k_z}\cos\beta\right)^2}}, \tag{3}$$

where β is the reflection azimuth, $|\mathbf{k_h}|$ is the absolute value of the offset wavenumber, k_{m_x} and k_{m_y} are the components of the midpoint wavenumber.

ARTIFACTS CAUSED BY SPARSELY SAMPLED WAVEFIELDS

As demonstrated in Rickett and Sava (2002), ADCIGs suffer from poor sampling of the source or receiver wavefield. This effect is not very obvious from the derivation in Sava and Fomel (2003); it is, however, more evident from the perspective of shot-profile migration. Appendix A analytically demonstrates that in locally constant-velocity media, when the receiver wavefield is densely sampled, the circular wavefronts of the downward continued receiver wavefields can be well reconstructed; hence the multi-offset imaging condition in equation (1) produces a linear relationship between subsurface half offset h_x and depth z for a specific CMP location x as follows:

$$z = -\tan\alpha x - \tan\gamma h_x, \qquad (4)$$

where α is the geological dip and γ is the reflection angle. If we take the derivative of z with respect to h_x, we get

$$\tan\gamma = -\frac{\partial z}{\partial h_x} = -\frac{k_{h_x}}{k_z}, \qquad (5)$$

which is exactly the same as equation (2). In other words, for well-sampled receiver wavefields, one shot will generate SODCIGs with a straight line. The slope of that line in local-offset domain is the tangent of the reflection angle γ. Hence, radial-trace or slant-stack transform in the subsurface-offset domain will produce artifact-free angle gathers, and a straight line in SODCIGs would be strictly mapped to a single point in the ADCIGs.

Let us consider the extreme case for poor sampling, where we have only one receiver. As demonstrated in Appendix B, when we have only one shot and one receiver, the multi-offset imaging condition in equation (1) no longer produces a linear relationship between subsurface half offset h_x and depth z. Instead z and h_x are non-linearly related as follows:

$$z^2 = -h_x^2 + (r-s)h_x + \frac{(r-s)^2}{\left[\tan(-\gamma-\alpha) + \tan(-\gamma+\alpha)\right]^2}, \qquad (6)$$

where s and r are the source location and receiver location respectively, and α is the geological dip. In such situations, the linear transformation from subsurface-offset domain to angle domain will definitely produce unwanted artifacts. Note that though here I limit my discussion to the effect in ADCIGs caused by poorly sampled receiver wavefields, reciprocity implies that the same should be true for poorly sampled source wavefields.

For example, Figure 1 shows a synthetic shot gather for a flat reflector at $z = 2000$ meters, with a constant velocity $v = 4000$ m/s. The shot is located at $x = -1000$ meters. For an image point at $x = 0$ meter, $z = 2000$ meters, the reflection angle should be $\gamma = \arctan(1000/2000) = 26.6°$. Figure 2(a) shows the migrated image obtained by using all the receivers shown in Figure 1. Figure 3(a) shows the SODCIG for surface location $x = 0$ meter; it shows a perfectly straight line intersecting at $(0, 2000)$ in the subsurface-offset domain (h_x, z). Figure 4(a) shows the ADCIG obtained by slant-stacking the corresponding SODCIGs in Figure 3(a). This result also shows a point located at about $26.6°$, which matches the theoretical result well. Figure

2(b), in contrast, shows the migration result obtained by using only one receiver located at $x = 1000$ meters. The image is an ellipse, which is basically a prestack impulse response. The SODCIG at $x = 0$ meter is shown in Figure 3(b), and as predicted by equation (6), it is a circle instead of a straight line in the subsurface-offset domain. The corresponding ADCIG is shown in Figure 4(b). Instead of a nicely focused point at 26.6°, we can identify a downward-frowning curve.

Figure 1: Synthetic shot gather for a flat reflector where the shot is located at $x = -1000$ meters. The modeling is done using finite difference. yaxun1-flat.shot [CR]
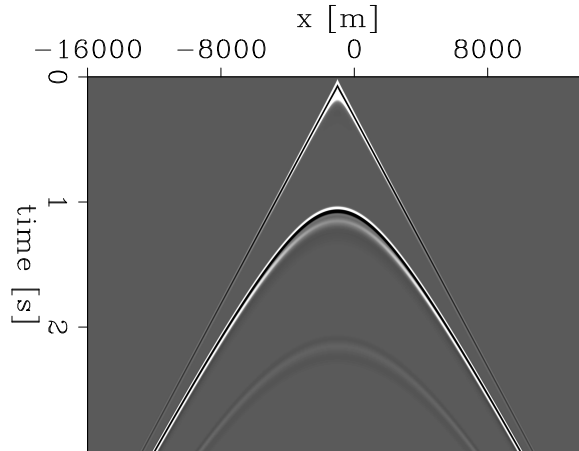
Figure 2: Migration results for only one shot. Panel (a) shows the migrated image for all the receivers shown in Figure 1, while (b) shows the migrated image for only one receiver located at $x = 1000$ meters. yaxun1-flat.img [CR]
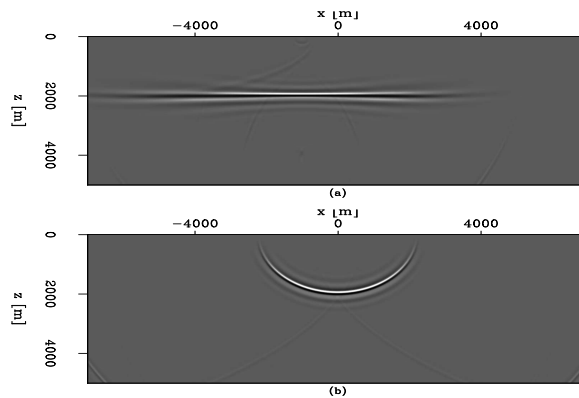
SELECTIVE STACKING BASED ON LOCAL SMOOTHING OF THE ENVELOPE FUNCTION

The downward-frowning artifacts observed in the previous section have a great influence on seismic angle-domain processing. They can destort the final image when we stack over the angle and azimuth axes, generating fake reflectors that can lead to misinterpretation. They can also affect the accuracy of residual-moveout-based velocity analysis, since with those frowning curves, it is difficult to predict the residual moveout acurately. There are four possible methods to get rid of those artifacts in angle gathers:

1. Define a non-linear transformation in the subsurface-offset domain to get an artifact-free angle gather.

Figure 3: SODCIGs at $x = 0$ meter for different results. (a) SODCIG extracted from the result in Figure 2(a), where a straight line is obtained, since the receiver wavefield is well sampled. (b) SODCIG extracted from the result in Figure 2(b), where a circle instead of a straight line is obtained, since the wavefield is extremely poorly sampled. yaxun1-flat.sodcig [CR]
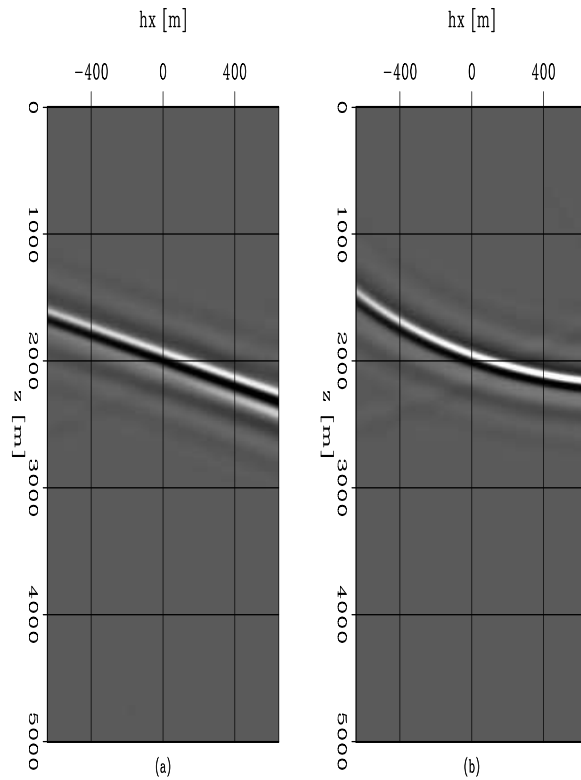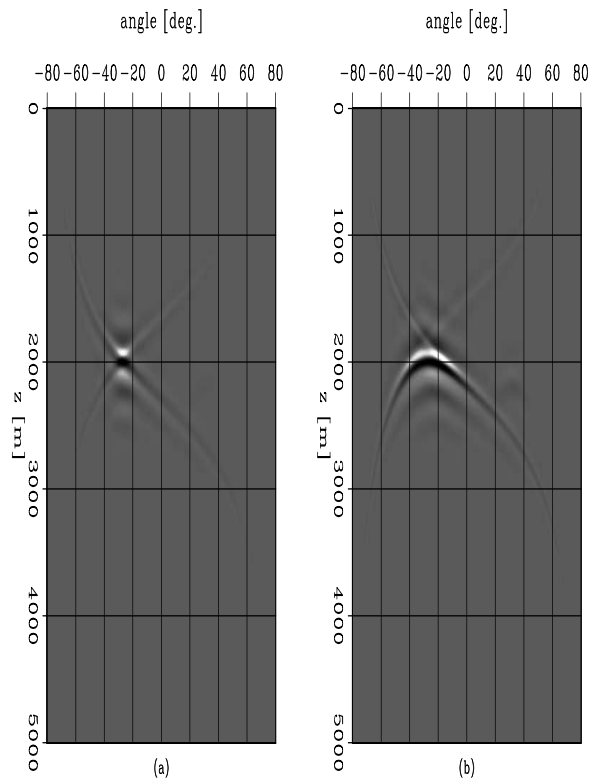
Figure 4: ADCIGs at $x = 0$ for different results. (a) ADCIG computed from Figure 3(a), where a nicely focused point at 26.6° is obtained, because the local offset gather in 3(a) is linear. (b) ADCIG computed from Figure 3(b), where a downward-frowning curve instead of a point is obtained, because the local-offset gather in 3(b) is non-linear. yaxun1-flat.adcig [CR]

2. Densely interpolate the data before migration. This data-space interpolation is very helpful if the velocity structure is simple, but helps little when the velocity structure is complex.

3. Apply image-space interpolation. By assuming that reflectivities are changing smoothly along angles and azimuths and that any abrupt changes in amplitudes are caused by poor illumination or poor sampling, we can run least-squares inversion with regularization in the angle domain by smoothing along angles and azimuths to attenuate those artifacts (Prucha et al., 2000). Or equivalently, we can run least-squares inversion with differential-semblence regularization in the subsurface-offset domain (Valenciano, 2006; Tang, 2006). Both these methods are effective but computationally demanding.

4. Apply selective stacking by designing filters or weighting functions that ignore those artifacts, stacking only angles and azimuths with good illumination and dense sampling.

In this paper, I will concentrate mainly on the fourth method and describe a simple but effective way to design the weighting functions. As we know, when migrating with the correct migration velocity and with densely sampled and infinite recording geometry, the events in ADCIGs are aligned horizontally. In 2-D there are horizontal lines in the angle domain; in 3-D there are flat planes in the angle and azimuth domain, because with infinite acquisition geometry, all angles and azimuths should be illuminated. When we don't have densely sampled and infinite recording geometry, there are holes in the line in the 2-D case or holes in the plane in the 3-D case. The shape of holes can be fairly irregular, depending on the recording geometry and the geological structure of the subsurface. The goal of the method is to attenuate the artifacts and enhance the signal-to-noise ratio of the final image by stacking only those angles and azimuths that are well illuminated. I first compute the envelope of the 3-D angle gather, then apply 3-D local smoothing based on equation (7) to the computed envelope to get the weighting function,

$$W(z,\gamma,\beta) = \frac{1}{2L+1} \sum_{j=-L}^{L} s(j)E(z+j\Delta z, \gamma+j\Delta\gamma, \theta+j\Delta\beta), \qquad (7)$$

where W is the weighting function for a particular CMP location. It is a function of depth z, reflection angle γ and reflection azimuth β. E is the envelope function, which can be computed via Hilbert transform. L is the half length of the moving window, and $s(j)$ determines the shape of the smoothing operator. In this paper I use a 3-D local boxcar smoothing operator, so $s(j) = 1$. A more sophisticated smoothing operator, such as a 3-D local Gaussian smoothing operator, could also be applied.

3-D SEG/EAGE SALT MODEL EXAMPLE

I tested the method discussed above on the 3-D wide-azimuth version of the SEG/EAGE salt data set. The wide-azimuth synthetic data was created by Sandia National Laboratory, it has 45 shots in total, with a shot interval of about 960 meters in both the inline and crossline directions. As can be seen in the plot of the shot layout in Figure 5, most of the shots are regularly

spaced, but some are not. The receiver geometry is a patching geometry, with minimum offset of about −2000 meters and maximum offset of about 2000 meters in both the inline and crossline directions. The plot of azimuth versus absolute offset is shown in Figure 6, which illustrates a fairly wide coverage of azimuth.

Figure 5: Shot layout. The horizontal axis is inline x, while the vertical axis is crossline y. Note most of the shots are regularly spaced, but several of them are not. yaxun1-segsalt.shot.layout [CR]
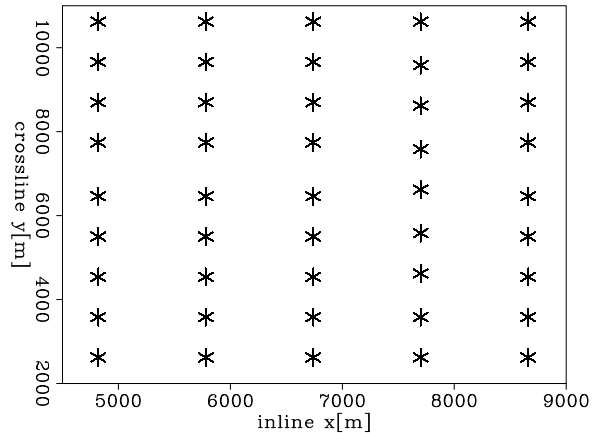
Figure 6: Azimuth vs. absolute offset plot. The horizontal axis is azimuth, while the vertical axis is absolute offset. This data set has very wide azimuth coverage. yaxun1-segsalt.off.azi [CR]
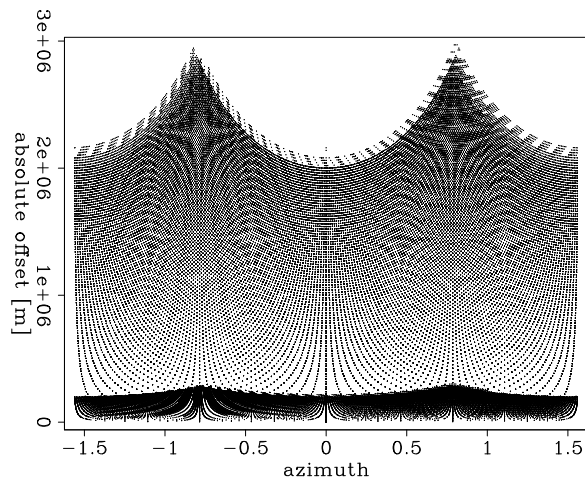
The migrated image obtained by using shot-profile migration for all 45 shots is shown in Figure 7. Since there are only 45 shots and they are sparsely distributed, the SODCIGs and ADCIGs should have significant sampling induced artifacts. To save disk space and computation cost, the SODCIGs are not computed for all the image points in the model space; instead, the output image coordinate is restricted to within [6580, 8480] for the inline direction and [8460, 9920] for the crossline direction. I computed 25 half-offsets for both the inline and crossline directions and the spacing of half-local-offset equals 40 meters, twice as much as the receiver spacing, which is 20 meters. Hence the half-subsurface-offset ranges from −480 meters to 480 meters in both the inline and crossline directions.

Figure 8 shows the migrated image for the particular image size discribed above. The crosshairs indicate two different surface locations for the output SODCIGs, which are shown in Figure 9. From Figure 9 we can see that since the correct migration velocity is used, there is some focusing of energy at zero offset. However, the energy is not well focused because
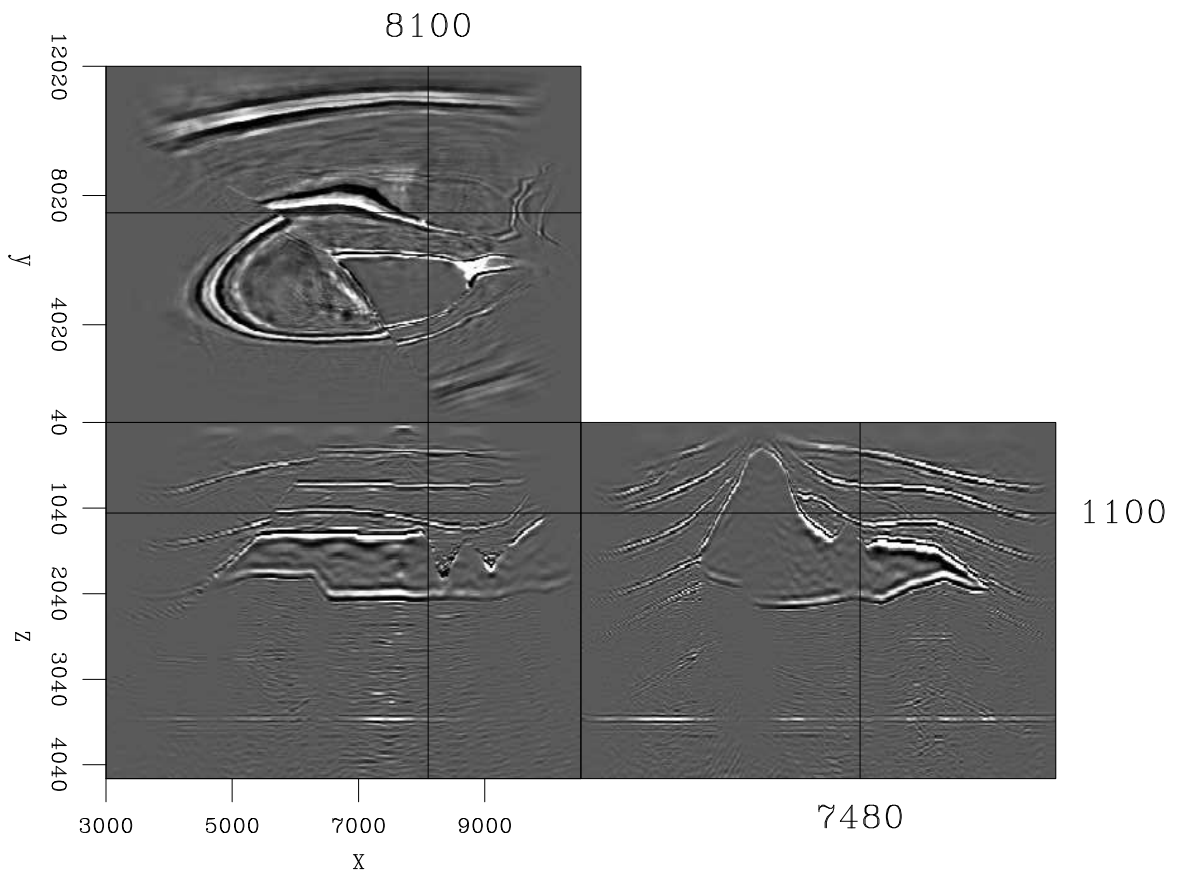
Figure 7: Shot-profile migration result of all 45 shots. yaxun1-segsalt.img [CR]

there are only 45 shots, and thus at most 45 planes intersecting at zero-offset location, which are not sufficient to cancel the energy at non-zero offsets.

Since the sources are extremely sparsely located, and the receiver coverage is limited for each shot, we can identify some curved events in the SODCIGs in Figure 9. For the events above the salt, the curvatures are not very obvious, because the velocity model above the salt is relatively simple; however, we can still see that some of the events are bending at far offsets. For events that are below the salt, the curvatures are more obvious, because with the complex salt body and limited recording geometry, it is impossible to have the receiver wavefield well sampled.
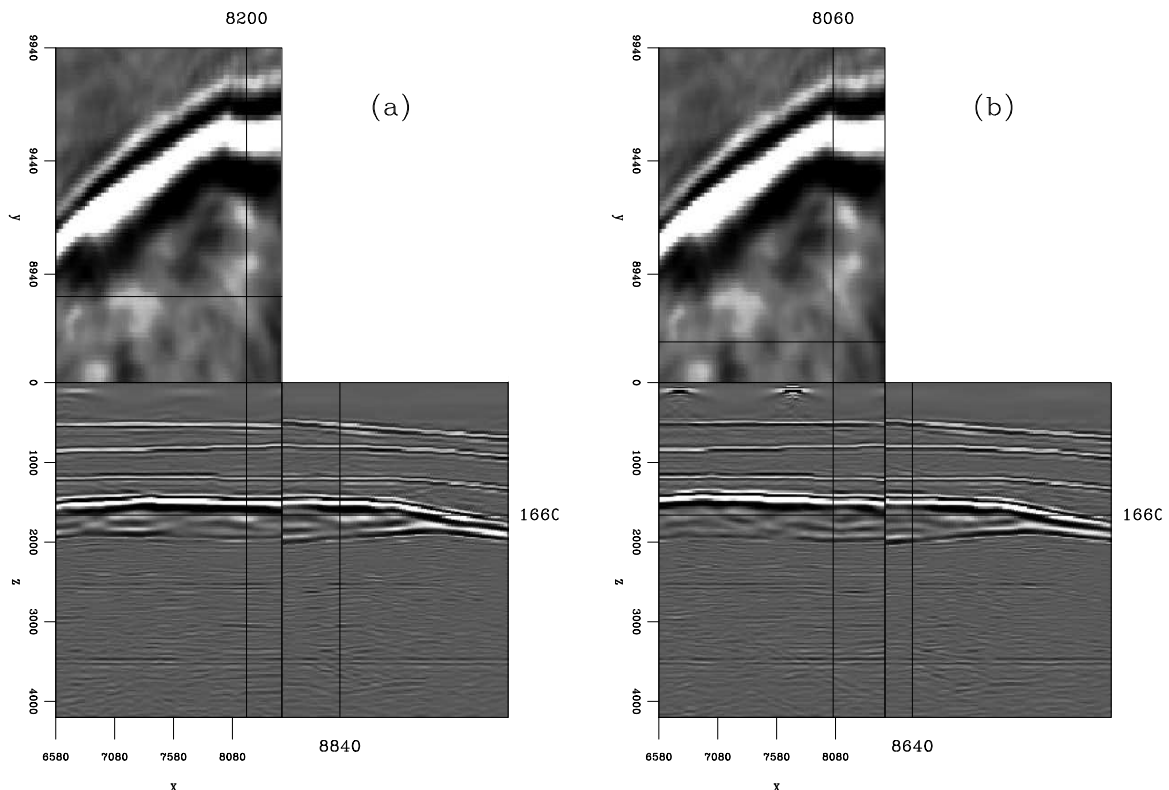

Figure 8: Migration result for the particular iamge size discribed in the text. The crosshairs indicate two different surface locations for output SODCIGs shown in Figure 9. (a) indicates the surface location at (8200, 8840); while (b) indicates the surface location at (8060, 8640). yaxun1-segsalt.off.loc [CR]

SODCIGs are transformed into 3-D ADCIGs by using equation (3). The corresponding ADCIGs are shown in Figure 10. The computed azimuth range is from 0 to 180 degrees with a spacing of 5 degrees. Note the blobs in the depth slices in both (a) and (b), which are closely related to the shot locations.

As demonstrated in the previous section, linear transformation from SODCIGs to AD-CIGs is prone to artifacts when the source or receiver wavefield is poorly sampled (sparsely distributed shot locations or receiver locations). Another possible reason for artifacts is large
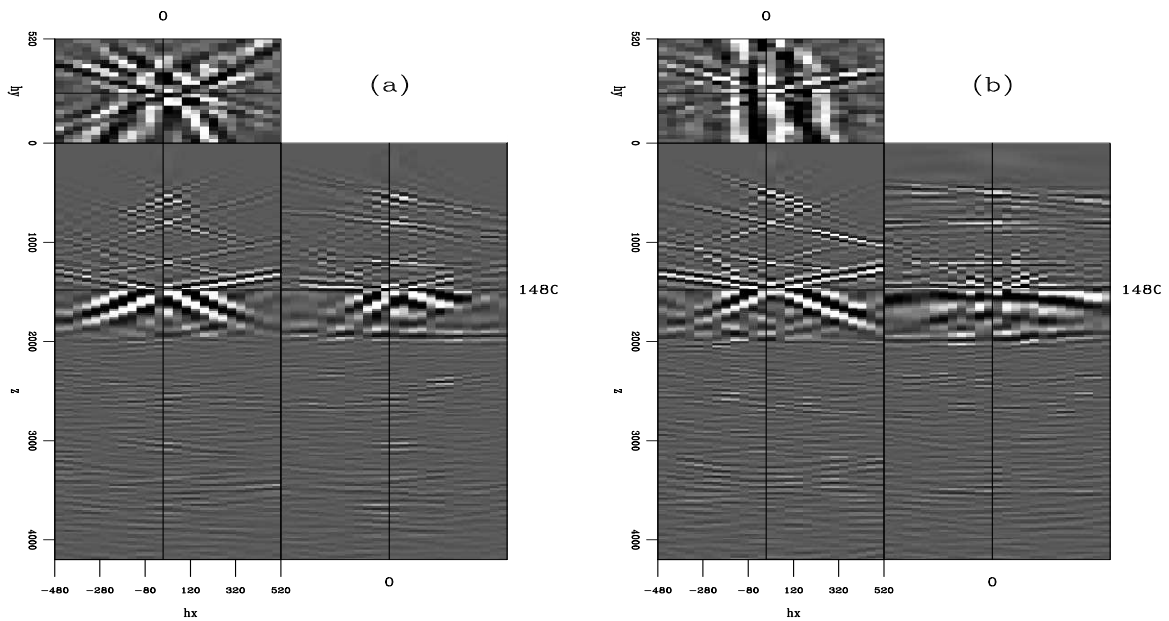
Figure 9: SODCIGs for two different surface locations shown in Figure 8. The left is the SOD-CIG extracted at $(8200, 8840)$, while the right is the SODCIG extracted at $(8060, 8640)$.The vertical axis in both figures is depth, the inline axis is h_x, and the crossline axis is h_y. yaxun1-segsalt.off [CR]
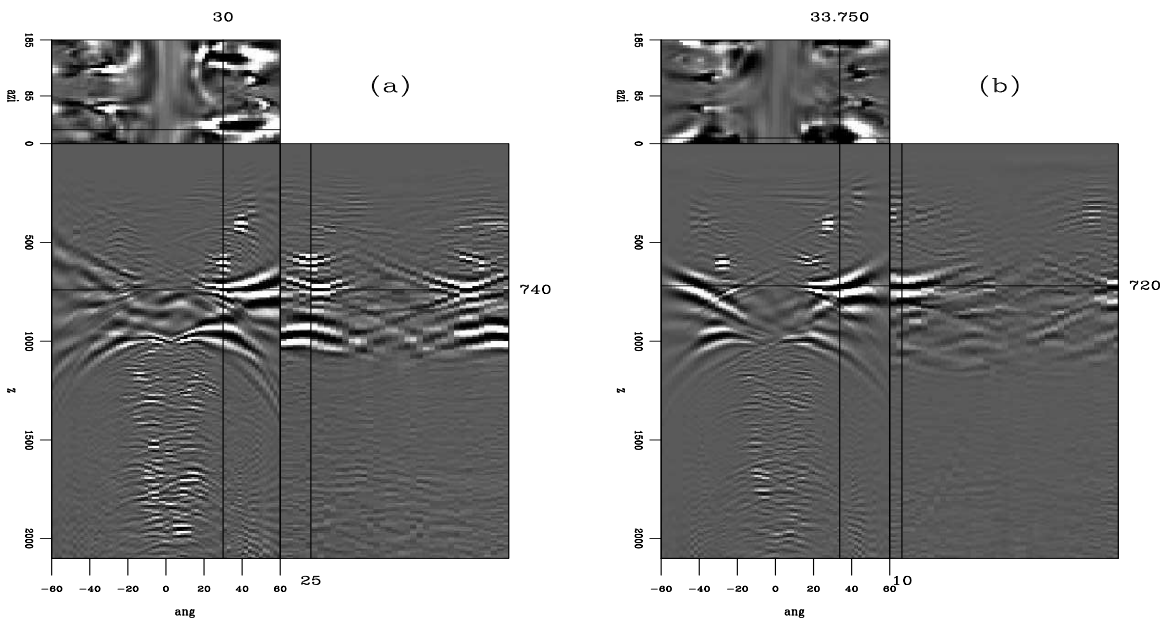

Figure 10: ADCIGs for two different surface locations shown in Figure 8. The left is the ADCIG extracted at $(8200, 8840)$, while the right is the SODCIG extracted at $(8060, 8640)$. The vertical axis in both figures is depth, the inline axis is reflection angle, and the crossline axis is reflection azimuth. yaxun1-segsalt.ang [CR]

velocity contrast in the vicinity of the image point, since the equations for subsurface-offset-to-angle transformation are valid only in media with locally constant velocity. Artifacts can be easily identified in ADCIGs for SEG/EAGE salt model as shown in Figure 10. We can find smeared energy (tails) in both near angles and far angles, especially in the top salt and base salt areas, where the velocity contrast is high, and in the subsalt area, where the wavefields are poorly sampled.

To form the final image cube, we have to stack the ADCIGs along both the reflection-angle and reflection-azimuth axes. As the transformation artifacts are not random, simple stacking without any weighting function might produce images with low signal-to-noise ratios, making interpretation difficult. The simply stacked image, shown in Figure 13(c), is quite noisy, especially in the subsalt. It is definitely difficult to interpret.

Instead of simply stacking along the angle and azimuth axes, we can apply weighting functions which attenuate unwanted artifacts to make the stacking process selective. The weighting functions are computed by using equation (7). Figure 11(b) shows the weighting function for the image point at $(8200, 8840)$, while Figure 12 shows the weighting function for the image point at $(8060, 8640)$. We can see that horizontally incoherent energy at near and far angles receives low weights, while horizontally coherent energy, where the actual reflection is located, receives high weights. Figure 11(c) and Figure 12(c) show the filtered results, in which the artifacts are greatly suppressed.

The weighting functions are computed for every image point and applied to the original ADCIGs, then the filtered ADCIGs are stacked together to form the final image. Figure 13(d) shows the result of using this kind of selective stacking. For comparison, Figure 13(a) shows the corresponding velocity model, Figure 13(b) shows the zero-offset image extracted from the SODCIG cube with $h_x = 0$ and $h_y = 0$, and Figure 13(c) shows the image obtained by simply stacking the ADCIGs without any weighting functions. It is quite obvious that the image in Figure 13(d), obtained by using selective stacking, has the highest signal-to-noise ratio and it is the cleanest among the three. Also notice the migration artifacts at the bottom of the image, which can be easily identified in Figures 13(b) and (c), but are greatly attenuated in Figure 13(d). The dipping reflector under the salt on the side panel, which is nearly invisible in Figure 13(b) and noisy in Figure 13(c), is clearly visible in Figure 13(d).

CONCLUSION AND DISCUSSION

I analytically demonstrated that when source or receiver wavefields are poorly sampled, subsurface-offset gathers are no longer linearly related to angle gathers. Slant-stack or radial-trace transform is prone to artifacts in such situations. This often happens when the underground velocity structure is very complex, since in complex geologies with limited recording geometries, it is difficult to have wavefields well sampled. To eliminate those artifacts, I presented a selective-stacking approach based on local smoothing of the envelope function. My test on the complex SEG/EAGE salt data set shows that by selectively stacking in the reflection angle and azimuth domain, a cleaner image with higher signal-to-noise ratio and less migration artifacts can be obtained.
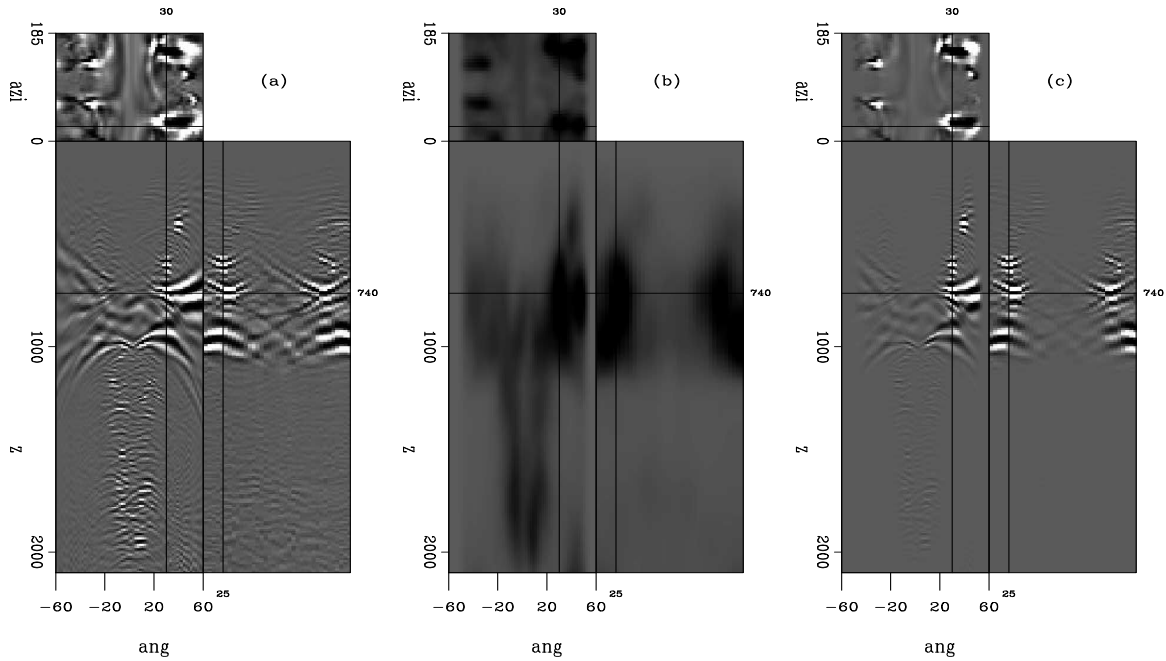
Figure 11: Filtering result for ADCIG at (8200, 8840). Panel (a) shows the original ADCIG, (b) is the computed weighting function via local smoothing of the envelope function, where dark color stands for high weight and light color stands for low weight. Panel (c) is (a) multiplied with (b), i.e. the filtered ADCIG. yaxun1-segsalt.ang-2.filt [CR]
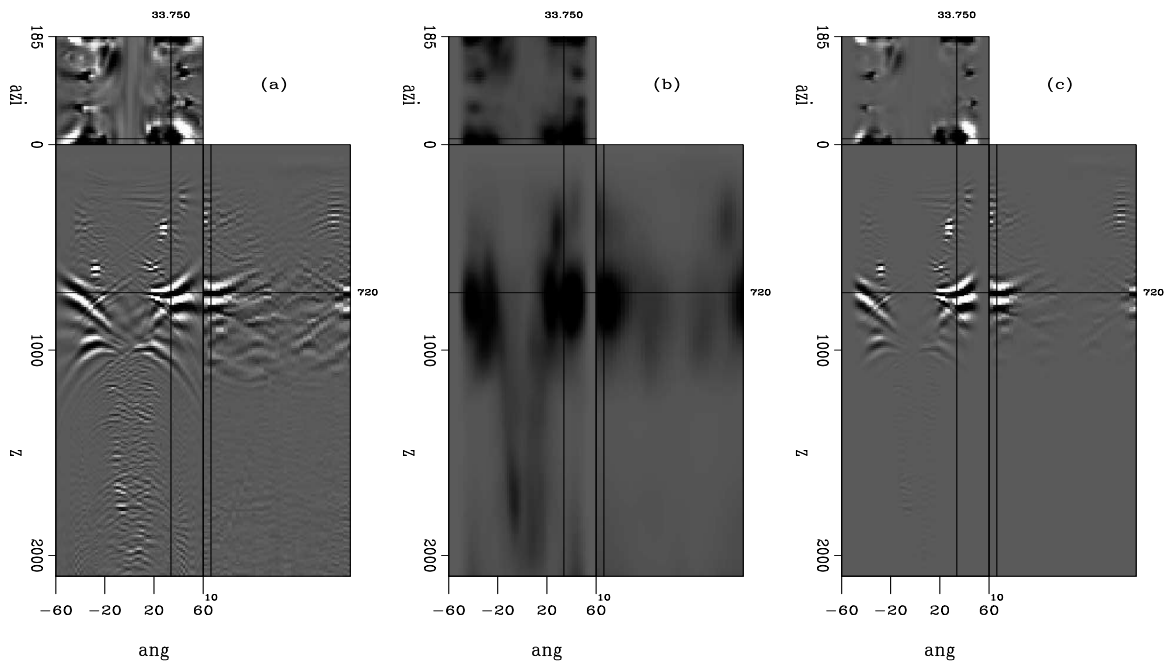

Figure 12: Filtering result for ADCIG at (8060, 8640). Panel (a) shows the original ADCIG, (b) is the computed weighting function via local smoothing of the envelope function, where dark color stands for high weight and light color stands for low weight. Panel (c) is (a) multiplied with (b), i.e. the filtered ADCIG. yaxun1-segsalt.ang-3.filt [CR]
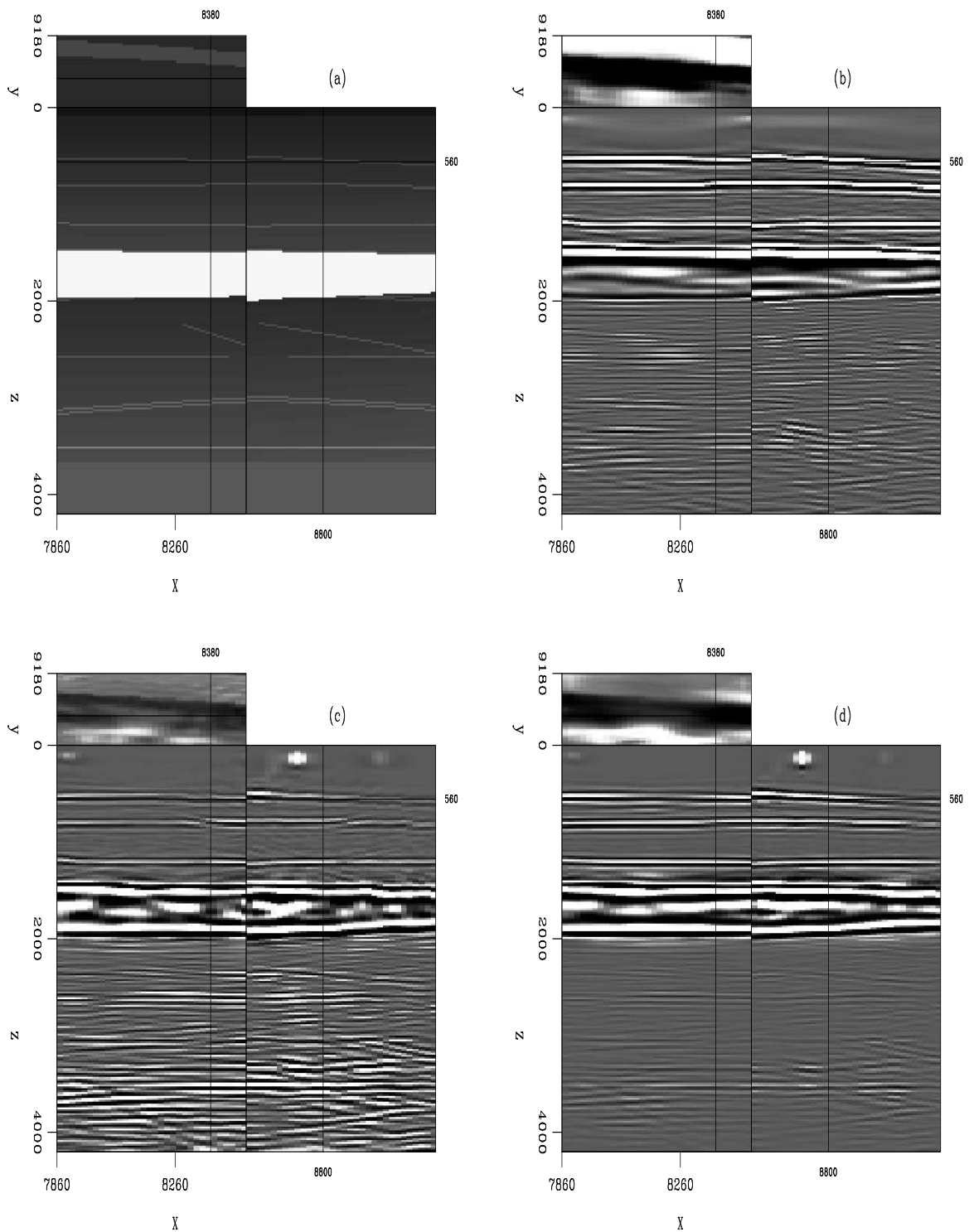
Figure 13: Comparison for different results. Panel (a) is the corresponding velocity model; (b) is the zero-offset image extracted from the SODCIG cube with $h_x = 0$ and $h_y = 0$; (c) is the result obtained by simple stacking without any weighting function; and (d) is the result obtained by selective stacking, with the weighting function computed by locally smoothing the envelope function of the ADCIGs. yaxun1-segsalt.stack [CR]

Though the method discussed in this paper is effective, it is purely based on signal processing. If the artifacts in the ADCIGs are coherent and strong, this signal-processing approach may not work well, because it tends to heavily weight strong energy. Instead, we can use the illumination of the subsurface as a reference for designing the weighting functions. The illumination can be measured in the least-square sense by computing the Hessian matrix. As illustrated in Valenciano and Biondi (2004), the Hessian is diagonal-dominated in well-illuminated areas, but the energy smears in areas that are not well illuminated, resulting in strong off-diagonal components. Therefore, the focus of energy in the diagonal of the Hessian can be a measure of illumination of the subsurface. We can further transform the Hessian into the reflection angle and azimuth domain, where well-illuminated reflection angles and azimuths will receive high energy, while poorly illuminated angles and azimuths will receive low energy. Therefore, we could design weighting functions based on the diagonal of the Hessian to attenuate unwanted artifacts and selectively stack those well-illuminated angles and azimuths to get a high-quality image. This methodology will be a future research topic.

ACKNOWLEDGMENTS

REFERENCES

Biondi, B. and G. Shan, 2002, Prestack imaging of overturned reflections by reverse time migration: 72nd Ann. Internat. Mtg., Soc. of Expl. Geophys., Expanded Abstracts, 1284–1287.

Biondi, B. and W. Symes, 2004, Angle-domain common-image gathers for migration velocity analysis by wavefield-continuation imaging: Geophysics, **69**, 1283–1298.

Howard, M. S. and N. Moldoveanu, 2006, Marine survey design for rich-azimuth seismic using surface streamers: 76rd Ann. Internat. Mtg., Soc. of Expl. Geophys., Expanded Abstracts, 2915–2919.

Keggin, J., T. Manning, et al., 2006, Key aspects of multi-azimuth acquisition and processing: 76rd Ann. Internat. Mtg., Soc. of Expl. Geophys., Expanded Abstracts, 2886–2890.

Michell, S., E. Shoshitaishvili, et al., 2006, Wide azimuth streamer imaging of mad dog: Have we solved the subsalt imaging problem?: 76rd Ann. Internat. Mtg., Soc. of Expl. Geophys., Expanded Abstracts, 2905–2909.

Mosher, C. and D. Foster, 2000, Common angle imaging conditions for prestack depth migration: 70th Ann. Internat. Mtg., Soc. of Expl. Geophys., Expanded Abstracts, 830–833.

Prucha, B. B., M. and W. Symes, 1999, Angle-domain common image gathers by wave-equation migration: 69th Ann. Internat. Mtg., Soc. of Expl. Geophys., Expanded Abstracts, 824–827.

Prucha, M. L., R. G. Clapp, and B. Biondi, 2000, Seismic image regularization in the reflection angle domain: SEP–**103**, 109–119.

Rickett, J. E. and P. C. Sava, 2002, Offset and angle-domain common image-point gathers for shot-profile migration: Geophysics, **67**, 883–889.

Sava, P. C. and S. Fomel, 2003, Angle-domain common-image gathers by wavefield continuation methods: Geophysics, **68**, 1065–1074.

Soubaras, R., 2003, Angle gathers for shot-record migration by local harmonic decomposition: 73rd Ann. Internat. Mtg., Soc. of Expl. Geophys., Expanded Abstracts, 889–892.

Tang, Y., 2006, Least-squares migration of incomplete data sets with regularization in the subsurface-offset domain:, **SEP-125**, 159–174.

Tisserant, T. and B. Biondi, 2003, Wavefield-continuation angle-domain common-image gathers in 3-D: SEP–**113**, 211–220.

Valenciano, A. A. and B. Biondi, 2004, Target-oriented computation of the wave-equation imaging Hessian: SEP–**117**, 63–76.

Valenciano, A. A., 2006, Target-oriented wave-equation inversion with regularization in the subsurface offset domain: SEP–**124**.

Xie, X. and R. Wu, 2002, Extracting angle domain information from migrated wavefield: 72nd Ann. Internat. Mtg., Soc. of Expl. Geophys., Expanded Abstracts, 1360–1363.

APPENDIX A

This appendix analytically derives SODCIGs for one shot and well-sampled receiver wavefields in locally constant-velocity media. Let's consider the SODCIG for a dipping reflector at image point (x_m, z_m), as shown in Figure (A-1). The dipping angle is $-\alpha$, while the reflection angle at (x_m, z_m) is $-\gamma$ (assuming positive sign for angles measured in a clockwise direction). The red circle shows the source wavefront at some time t, which intersects the dipping reflector at (x_m, z_m). If we put receivers for every location on the surface, i.e. the receiver wavefield is sufficiently densely sampled, when we downward continue or backward propagate the receiver wavefield, the circular wavefront, which is in blue, can be well reconstructed. It also intersets the dipping reflector at (x_m, z_m) at the same time t. Therefore, cross-correlation of the source wavefield and receiver wavefield will generate the image at (x_m, z_m).

Figure A-1: When the receiver wavefield is sufficiently densely sampled, the actual circular wavefront in blue can be well reconstructed. yaxun1-dip.full.rec [NR]
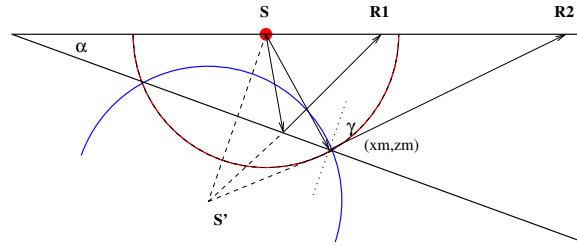
The equation for the source wavefront in red is

$$(x - s)^2 + z^2 = \left[\frac{(x_m - s)}{\sin(-\gamma + \alpha)} \right]^2, \tag{A-1}$$

while the equation for the receiver wavefront in blue is

$$[x - s\cos(-2\alpha)]^2 + [z - s\sin(-2\alpha)]^2 = \left[\frac{(x_m - s)}{\sin(-\gamma + \alpha)} \right]^2. \tag{A-2}$$

To get the local offset gather at x_m, we have to apply the multi-offset imaging condition described in equation (1) as follows, where h is the subsurface half-offset.

$$\begin{cases} (x - h - s)^2 + z^2 = \left[\frac{(x_m - s)}{\sin(-\gamma + \alpha)} \right]^2 \\ [x + h - s\cos(-2\alpha)]^2 + [z - s\sin(-2\alpha)]^2 = \left[\frac{(x_m - s)}{\sin(-\gamma + \alpha)} \right]^2 \end{cases} \tag{A-3}$$

Therefore, by letting $x = x_m$ and subtracting the second equation from the first equation, we get

$$(x_m - h - s)^2 + z^2 = [x_m + h - s\cos(-2\alpha)]^2 + [z - s\sin(-2\alpha)]^2. \tag{A-4}$$

After some algebra, we get

$$[2x_m - s(1 + \cos(-2\alpha))][s(\cos(-2\alpha) - 1) - 2h] + (2z - s\sin(-2\alpha))s\sin(-2\alpha) = 0. \tag{A-5}$$

Rearranging the above equation:

$$z = \frac{x_m s \sin^2(-\alpha) + x_m h - hs \cos^2(-\alpha)}{s \cos(-\alpha)\sin(-\alpha)} \tag{A-6}$$

$$= \tan(-\alpha)x_m + \frac{x_m - s\cos^2(-\alpha)}{s\cos(-\alpha)\sin(-\alpha)}h \tag{A-7}$$

$$= -\tan\alpha\, x_m + \frac{\frac{x_m}{s} - \cos^2(-\alpha)}{\cos(-\alpha)\sin(-\alpha)}h. \tag{A-8}$$

From Figure (A-1), point (x_m, z_m) on the dipping reflector satisfies:

$$\tan(-\gamma + \alpha) = \frac{x_m - s}{z_m} \tag{A-9}$$

$$\tan(-\alpha) = \frac{z_m}{x_m}. \tag{A-10}$$

Multiplying them together yields

$$\tan(-\alpha)\tan(-\gamma+\alpha) = \frac{x_m - s}{x_m} = \frac{\frac{x_m}{s} - 1}{\frac{x_m}{s}}, \tag{A-11}$$

so

$$\frac{x_m}{s} = \frac{1}{1 - \tan(-\alpha)\tan(-\gamma+\alpha)}. \tag{A-12}$$

Substituting equation(A-12) into equation (A-8), we get:

$$z = -\tan\alpha\, x_m + \frac{\frac{x_m}{s} - \cos^2(-\alpha)}{\cos(-\alpha)\sin(-\alpha)}h \tag{A-13}$$

$$= -\tan\alpha\, x_m + \frac{\frac{1}{1-\tan(-\alpha)\tan(-\gamma+\alpha)} - \cos^2(-\alpha)}{\cos(-\alpha)\sin(-\alpha)}h \tag{A-14}$$

$$= -\tan\alpha\, x_m + \frac{1 - \cos^2(-\alpha)[1 - \tan(-\alpha)\tan(-\gamma+\alpha)]}{[1 - \tan(-\alpha)\tan(-\gamma+\alpha)]\cos(-\alpha)\sin(-\alpha)}h \tag{A-15}$$

$$= -\tan\alpha\, x_m + \frac{\sin^2(-\alpha) + \sin(-\alpha)\cos(-\alpha)\tan(-\gamma+\alpha)}{\sin(-\alpha)\cos(-\alpha) - \sin^2(-\alpha)\tan(-\gamma+\alpha)}h \tag{A-16}$$

$$= -\tan\alpha\, x_m + \frac{\sin(-\alpha) + \cos(-\alpha)\tan(-\gamma+\alpha)}{\cos(-\alpha) - \sin(-\alpha)\tan(-\gamma+\alpha)}h \tag{A-17}$$

$$= -\tan\alpha\, x_m + \frac{\tan(-\alpha) + \tan(-\gamma+\alpha)}{1 - \tan(-\alpha)\tan(-\gamma+\alpha)}h \tag{A-18}$$

$$= -\tan\alpha\, x_m + \tan(-\alpha - \gamma + \alpha)h \tag{A-19}$$

$$= -\tan\alpha\, x_m - \tan\gamma\, h. \tag{A-20}$$

Actually the above equation is true for each point (x, z) with dipping angle α and opening angle γ, so it can be rewritten as follows:

$$z = -\tan\alpha\, x - \tan\gamma\, h. \tag{A-21}$$

Therefore, when the receiver wavefield is sufficiently densely sampled, the SODCIG is linearly related to the angle gather.

APPENDIX B

This appendix analytically derives SODCIGs for one shot and one receiver in locally constant-velocity media. Let's again consider a dipping reflector with the dip angle α, as shown in Figure B-1. The source is located at $(s,0)$, while receiver is located at $(r,0)$. Since there is only one receiver, when we downward continue or backward propagate the receiver wavefield, the receiver wavefront that intersects (x_m, z_m) is the green one shown in Figure B-1 instead of the blue one shown in Figure A-1.
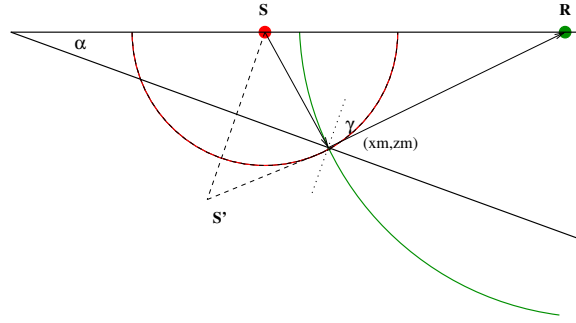

Figure B-1: In the extreme situation where there is only one receiver, the receiver wavefront is the one shown here in green, instead of the blue one shown in Figure A-1.
yaxun1-dip.one.rec [NR]

The image point at (x_m, z_m) on the dipping reflector certainly satisfies:

$$\tan(-\gamma + \alpha) = \frac{x_m - s}{z_m} \tag{B-1}$$

$$\tan(-\gamma - \alpha) = \frac{r - x_m}{z_m}. \tag{B-2}$$

Thus, we have:

$$z_m = \frac{x_m - s}{\tan(-\gamma + \alpha)} = \frac{r - x_m}{\tan(-\gamma - \alpha)}, \tag{B-3}$$

which rearranges to

$$x_m = \frac{s\tan(-\gamma - \alpha) + r\tan(-\gamma + \alpha)}{\tan(-\gamma - \alpha) + \tan(-\gamma + \alpha)}. \tag{B-4}$$

Since (x_m, z_m) is the intersecting point of the source wavefront and the receiver wavefront, it should satisfy the source wavefront equation:

$$(x - s)^2 + z^2 = \left[\frac{x_m - s}{\sin(-\gamma + \alpha)}\right]^2, \tag{B-5}$$

and the receiver wavefront equation:

$$(x - r)^2 + z^2 = \left[\frac{r - x_m}{\sin(-\gamma - \alpha)}\right]^2. \tag{B-6}$$

To get the SODCIG, we have to apply the multi-offset imaging conditon described in equation (1) as follows, where h is the subsurface half-offset,

$$\begin{cases} (x-h-s)^2 + z^2 = \left[\frac{(x_m-s)}{\sin(-\gamma+\alpha)}\right]^2, \\ (x+h-r)^2 + z^2 = \left[\frac{(x_m-r)}{\sin(-\gamma-\alpha)}\right]^2. \end{cases} \tag{B-7}$$

Therefore, by letting $x = x_m$ and summing the above two equations together, we can derive the relationship between z and h for surface location x_m:

$$(x_m-h-s)^2 + (x_m+h-r)^2 + 2z^2 = \left[\frac{x_m-s}{\sin(-\gamma+\alpha)}\right]^2 + \left[\frac{r-x_m}{\sin(-\gamma-\alpha)}\right]^2 \tag{B-8}$$

From equation (B-4), it is easy to get:

$$x_m - s = \frac{s\tan(-\gamma-\alpha) + r\tan(-\gamma+\alpha)}{\tan(-\gamma-\alpha) + \tan(-\gamma+\alpha)} - s = \frac{(r-s)\tan(-\gamma+\alpha)}{\tan(-\gamma-\alpha) + \tan(-\gamma+\alpha)} \tag{B-9}$$

and

$$r - x_m = r - \frac{s\tan(-\gamma-\alpha) + r\tan(-\gamma+\alpha)}{\tan(-\gamma-\alpha) + \tan(-\gamma+\alpha)} = \frac{(r-s)\tan(-\gamma-\alpha)}{\tan(-\gamma-\alpha) + \tan(-\gamma+\alpha)}, \tag{B-10}$$

Substituting equations (B-9) and (B-10) into equation (B-8), after some algebra, we get

$$z^2 = -h^2 + (r-s)h + \frac{(r-s)^2}{\left[\tan(-\gamma-\alpha) + \tan(-\gamma+\alpha)\right]^2}. \tag{B-11}$$

Obviously, in this situation, depth z is not linearly related to subsurface half-offset h. When $\alpha = 0$, i.e. for a flat reflector, the above equation can be simplified as follows:

$$z^2 = -h^2 + (r-s)h + \frac{(r-s)^2}{4\tan^2\gamma}. \tag{B-12}$$